Exp Fluids (2012) 53:145–162
DOI 10.1007/s00348-012-1275-7

RESEARCH ARTICLE

Experimental study of stratified jet by simultaneous measurements of velocity and density fields

Duo Xu · Jun Chen

Received: 10 May 2011 / Revised: 26 November 2011 / Accepted: 31 January 2012 / Published online: 29 February 2012

Abstract Stratified flows with small density difference commonly exist in geophysical and engineering applications, which often involve interaction of turbulence and buoyancy effect. A combined particle image velocimetry (PIV) and planar laser-induced fluorescence (PLIF) system is developed to measure the velocity and density fields in a dense jet discharged horizontally into a tank filled with light fluid. The illumination of PIV particles and excitation of PLIF dye are achieved by a dual-head pulsed Nd:YAG laser and two CCD cameras with a set of optical filters. The procedure for matching refractive indexes of two fluids and calibration of the combined system are presented, as well as a quantitative analysis of the measurement uncertainties. The flow structures and mixing dynamics within the central vertical plane are studied by examining the averaged parameters, turbulent kinetic energy budget, and modeling of momentum flux and buoyancy flux. At downstream, profiles of velocity and density display strong asymmetry with respect to its center. This is attributed to the fact that stable stratification reduces mixing and unstable stratification enhances mixing. In stable stratification region, most of turbulence production is consumed by mean-flow convection, whereas in unstable stratification region, turbulence production is nearly balanced by viscous dissipation. Experimental data also indicate that at downstream locations, mixing length model performs better in mixing zone of stable stratification regions, whereas in other regions, eddy viscosity/diffusivity models with static model coefficients represent effectively momentum and buoyancy flux terms. The measured turbulent Prandtl number displays strong spatial variation in the stratified jet.

D. Xu · J. Chen (✉)
School of Mechanical Engineering, Purdue University,
West Lafayette, IN 47907, USA
e-mail: junchen@purdue.edu

1 Introduction

Stratified flows with small density difference exist extensively in environmental and engineering applications. Ocean dynamics is described as thin stratified flow using hydrostatic and Boussinesq approximations (e.g., Smith et al. 2010). Oceanic overflows are of particular interest, where currents with slight density difference mix. For example, in Denmark Strait Overflow, the cold current from Nordic Seas starts to mix with warm seawater in Atlantic ocean. This local flow phenomenon (stratified and including not fully developed regime) is the driving mechanism of global thermohaline "conveyor belt" circulation (Bacon 1998; Hansen and Østerhus 2000). Thus, accurate modeling of this stratified mixing process is important for predicting ocean/climate evolution. Other examples of stratified flows include various forms of gravity current, discharge of sewage water into open water body, hot exhausted gas released via chimney stacks, as well as flows in HVAC (Heating, Ventilating, and Air Conditioning) applications. The recent oil-spill in Gulf of Mexico is in nature an immiscible stratified jet.

When density difference is small, Boussinesq assumption can be applied in non-dimensional momentum equation,

$$\frac{\partial U_j^*}{\partial t^*} + U_i^* \frac{\partial U_j^*}{\partial x_i^*} = -\frac{\partial {P_d}^*}{\partial x_j^*} + \frac{1}{Re}\frac{\partial^2 U_j^*}{\partial x_i^* \partial x_i^*} + Ri \cdot \theta \cdot \delta_{j3}, \qquad (1)$$

where the superscript "*" denotes non-dimensional parameters, for example, $U_j^* = U_j/U_o$, $P_d^* = P_d/(\rho U_o^2)$ and $x_j^* = x_j/D$ are non-dimensional velocity, pressure and coordinates, respectively, and $\theta(\mathbf{x}, t) = \rho_d(\mathbf{x}, t)/\rho_{d_o}$ is

non-dimensional density difference, where U_o, D, and ρ_{d_o} are characteristic velocity, length scale, and dynamic density difference, respectively. $Re = U_o D/\nu$ and $Ri = g'D/U_o^2$ are Reynolds and Richardson numbers, in which $g' = g\rho_{d_o}/\rho$ is the reduced gravity. As shown in Eq. 1, the dynamics of stratified flows is governed by both viscous effect and buoyant effect. Furthermore, $\theta(\mathbf{x}, t)$ is governed by its own equation:

$$\frac{\partial\theta}{\partial t} + U_i\frac{\partial\theta}{\partial x_i} = \kappa\frac{\partial^2\theta}{\partial x_i\partial x_i}, \tag{2}$$

where κ is the mass diffusivity.

When Reynolds-Averaged approach is used to study stratified flows, the flow parameters are decomposed into mean part and fluctuating part: $U_j = \langle U_j\rangle + u_j$, $P = \langle P\rangle + p$, and $\theta = \langle\theta\rangle + \theta'$. The Reynolds stress $-\rho\langle u_i u_j\rangle$ and density flux $g'\langle\theta' u_j\rangle$ must be appropriately modeled in order to close the equations. In stratified flows, the vertical momentum flux and density flux are of special interests and usually modeled using turbulent eddy viscosity κ_v and eddy diffusivity κ_ρ (e.g., Thorpe 2007), i.e.,

$$\langle u_1 u_3\rangle = -\kappa_v\frac{\partial\langle U_1\rangle}{\partial x_3}, \tag{3}$$

$$\langle\theta' u_3\rangle = -\kappa_\rho\frac{\partial\langle\theta\rangle}{\partial x_3}, \tag{4}$$

from which the turbulent Prandtl number $Pr_T = \kappa_v/\kappa_\rho$ is defined.[1] Despite the wide use of the hypotheses, the attempts to measure Pr_T experimentally in stratified flows are limited. In addition, for large-scale numerical simulations where the cost of achieving ideal resolution is formidably large, developing simple yet effective sub-grid scale parameterization models, for terms like $\langle u_1 u_3\rangle$ and $\langle\theta' u_3\rangle$, presents a major challenge. It requires sound understanding of the underlying physics of the mixing processes in stratified environment, as well as their interplay with turbulence (e.g., Large et al. 1994; Ivey et al. 2008; Stretch et al. 2010; Muller and Garrett 2002).

Extensive laboratory experiments of stratified flows have been conducted over the years, from the early ones using a tilted tank that lead to the Morton–Taylor–Turner entrainment assumption (Ellison and Turner 1959; Turner 1986). Pouliquen et al. (1994) study the interface between two immiscible constant-density fluids in a tilted tank experiment. Recent studies focus on eddy formation and mixing structures (Hallworth et al. 1993; Kneller et al. 1999; Baines 2001, 2002, 2005; Sutherland 2002). One may refer to Simpson (1997), Lowe et al. (2002), Thomas and Linden (2007), Ivey et al. (2008) and references therein for a list of additional laboratory experiments. In portion of these experiments, visualization techniques, such as use of color dye, have been applied for qualitative measurements of bulk parameters like the current thickness, whereas others use quantitative measurement techniques, e.g., hot-wire anemometer (HWA) and laser Doppler velocimetry (LDV). Particle image velocimetry (PIV) is applied to measure flow structures in stratified flow (e.g., Webster and Liu 2001; Kwon and Seo 2005). PIV is also applied by Spedding et al. (1996) to study the wakes of towed spheres in a stably stratified fluid, and it is reported that the late stages of a even weakly stratified wake will be fully controlled by buoyancy (Spedding 1997). Planar laser-induced fluorescence (PLIF) is used to study the entrainment and mixing mechanism where concentration of PLIF dye serves as a surrogate of scalar field (e.g., Dahm and Dimotakis 1987; Crimaldi and Koseff 2001; Troy and Koseff 2005). Papanicolaou and List (1998) combine PLIF and LDV to measure the velocity field and concentration distribution in buoyant jet and plume. Different combinations of PIV and PLIF are reported to measure the scalar and velocity field simultaneously to gain understanding of turbulent mixing by examining the scalar fluxes (e.g., Wang 2000; Borg et al. 2001; Hjertager et al. 2003; Feng et al. 2007). A single-camera coupled particle tracking velocimetry (PTV) and PLIF technique is used to study the round turbulent jet and transport of buoyant fluid (Cowen et al. 2001; Horner-Devine 2006). Hult et al. (2009) apply combined PIV/PLIF using the Argon-ion laser and scanning mirror to study the instability of waves breaking at the ridge. Another combined PIV and PLIF system is developed to measure velocity and density in a 2D density current, where focus is on full-field measurements of high-Reynolds number gravity current generated through a turbulence enhancement mechanism (Chen et al. 2007; Odier et al. 2009).

Nevertheless, all the aforementioned experiments provide valuable data sets for investigation of small-scale flow structure and mixing dynamics. However, more experiments on stratified flows are still needed with the ability to examine the momentum and scalar fluxes as well as the implications in developing models for numerical simulations. In this paper, we present an experimental study of a horizontally introduced turbulent stratified jet, in which the dominant buoyancy flux occurs in vertical direction, whereas the dominant turbulent momentum flux is along horizontal direction. This problem represents a simplified model to study the interaction of turbulence and stratification. Particularly, studying this stratified jet in the near-nozzle region has implication in modeling the not-fully

[1] The eddy diffusivity of heat, κ_T, and eddy diffusivity of density, κ_ρ, are equal when density variations are dominated by those of temperatures, as in many applications. Details can be found in Thorpe (2007, e.g., p. 42). Thus here we do not differentiate κ_T and κ_ρ, as well as turbulent Prandtl nubmer and turbulent Schimidt number.

developed regimes. This work is motivated by the need of studying stratified mixing using measured velocity and density data at high-resolution. In addition, studying the flow structures and dynamics helps to identify easy-to-implement yet accurate models in large-scale simulations, in which application of advanced models is limited by available computation resources.

The paper is organized as follows: details of the experimental apparatus are presented in Sect. 2. Instrumentation system is introduced in Sect. 3. The experimental conditions are characterized in Sect. 4. In Sect. 5, the results are discussed. The final section gives a summary and outlook.

2 Facility

The core part of the facility consists of a main tank and a jet nozzle as shown in Fig. 1. The main tank, of dimensions $110 \times 30 \times 25$ cm^3, is made of 1.27-cm-thick acrylic plates and is filled with light fluid (ethanol solution, density ρ_e). The jet nozzle is composed of diffuser, settling chamber, and contraction sections, as shown in Fig. 1. Its design follows the principle discussed by Mehta and Bradshaw (1979) for designing wind tunnel. The jet nozzle reduces flow fluctuation to generate a stable flow profile at the nozzle exit ($x/D = 0$), as shown in Fig. 1, where the inside diameter is $D = 1.27$ cm. It is manufactured by 3D jet printing technique and is connected to an acrylic tube as shown in Fig. 1. A constant head system (not shown in Fig. 1), composed of a head-control tank, a supply tank, and two centrifugal pumps, is filled with dense fluid (salt solution, density ρ_s). Another centrifugal pump connected to the constant head system generates a jet of dense fluid into the light fluid in the main tank with different Richardson numbers at different experiments. A flowmeter is connected to the inlet of the nozzle to control the inject flow rate. Also as shown in Fig. 1, a piece of polycarbonate honeycomb (thickness 7.5 cm, hole diameter 3 mm) is placed at the far end of the tank to reduce the secondary flow reflected by the end wall. Another piece of honeycomb (thickness 5.0 cm, hole diameter 3 mm) is placed in the main tank to eliminate the surface wave. The origin of the coordinate system is set at the center of the jet exit plane, shown in Fig. 1. x-axis (x_1) is set horizontally along the flow direction. y-axis (x_2) is set to be perpendicular to the x-axis in the horizontal plane. z-axis (x_3) points upwardly and is antiparallel to gravitional direction.

This facility enables us to study the characteristics of a horizontal stratified turbulent jet, in which both stable stratification and unstable stratification are observed. Stable stratification is formed where the light fluid is on top of dense fluid (Fig. 1, with stable local density gradient: $d\rho/dx_3 < 0$, also as illustrated in Fig. 2a). On the contrary, unstable stratification is formed where the dense fluid is on top of light fluid (unstable local density gradient: $d\rho/dx_3 > 0$, Fig. 2b). In stable stratification region, mixing caused by turbulent perturbation is reduced due to the restoring mechanism from buoyancy force. In unstable stratification region, on the contrary, mixing caused by turbulent perturbation is enhanced by the destructive influence of buoyancy force.

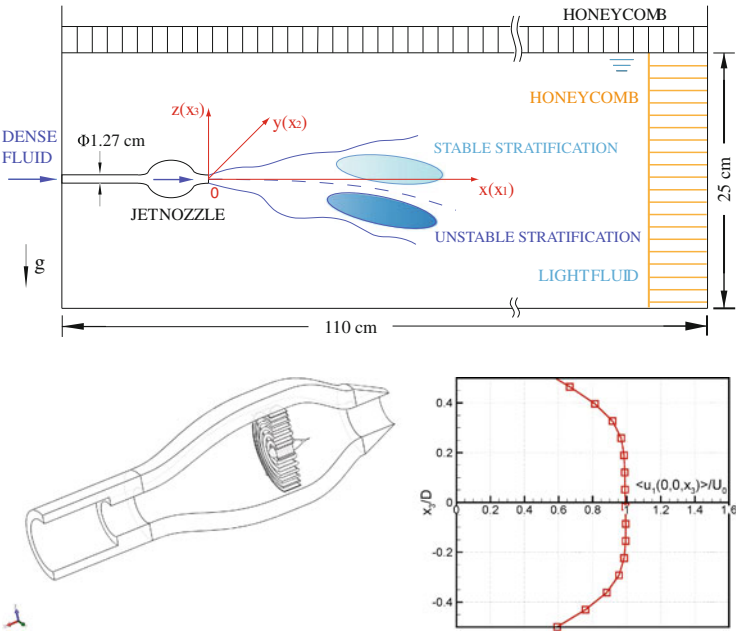

Fig. 1 (*Top*) schematics of the stratified jet facility. (*Bottom left*) cross-sectional view of the jet nozzle, and (*bottom right*) mean streamwise velocity at the nozzle exit ($x/D \simeq 0$)

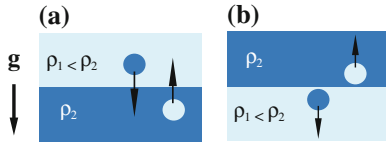

Fig. 2 Schematic illustrations of **a** stable stratification and **b** unstable stratification. *Arrows* show the buoyancy force applied on a fluid element when it deviates from its original position by disturbance

3 Instrumentation

A combined PIV-PLIF system is developed for measuring the velocity and density fields simultaneously at different downstream locations of the stratified jet along the central vertical plane ($x_2 = 0$), as shown in Fig. 3.

3.1 Matching the refractive indices

When optical flow diagnostics techniques are applied in stratified flows, the refractive indices of the dense fluid and light fluid must be accurately matched (McDougall 1979; Hannoun et al. 1988; Alahyari and Longmire 1994; Daviero et al. 2001). Otherwise, a slight difference of refractive indices, associated with the density difference between two fluids, results in unfocused images through the optical recording system and significantly deteriorates the accuracy of the measurements. In the present work, the densities and refractive indices of both fluids are measured by a densitometer (Mettler Toledo Densito 30PX) and a refractometer (Mettler Toledo Refracto 30PX), respectively. In the range of our interest, the refractive index and density have a nearly linear relationship for each liquid, as shown in Fig. 4. For a chosen density difference, ρ_e and ρ_s can then be determined from the two curves (Fig. 4).

3.2 Measuring velocity field using PIV

The dense and light fluids are uniformly seeded with hollow glass beads (median diameter 11 μm, specific gravity 1.1) for PIV measurement. A twin-head Nd:YAG pulse laser (532 nm, peak energy 130 mJ/pulse) illuminates the test section by forming a 1-mm-thick laser sheet through a group of optics (Fig. 3). A CCD camera (14-bit Imager ProX 4M camera) of $2,112 \times 2,072$ pixels resolution records particle images, operated under double exposure mode at a sampling rate of 5 Hz. The time delay between the two pulses is set from hundreds of microseconds to few milliseconds, depending on the averaged flow velocity in the sample area. Velocity vectors are retrieved by processing image pairs using PIV analysis software (Davis 7.0). A two-step processing is applied: 64×64 pixels interrogation window and 50% overlap for the first step,

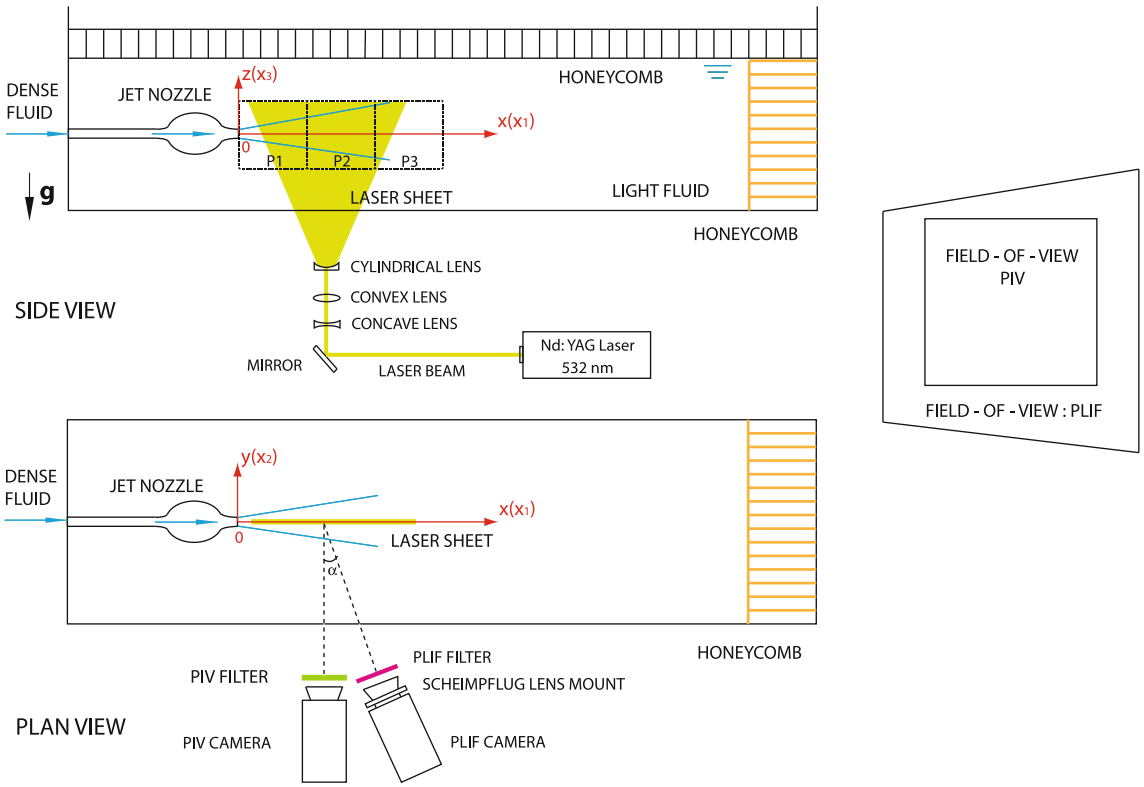

Fig. 3 Combined PIV-PLIF system for measuring velocity and density in vertical ($x_1 - x_3$) plane. Also shown is the effective field-of-view of PIV and PLIF measurements

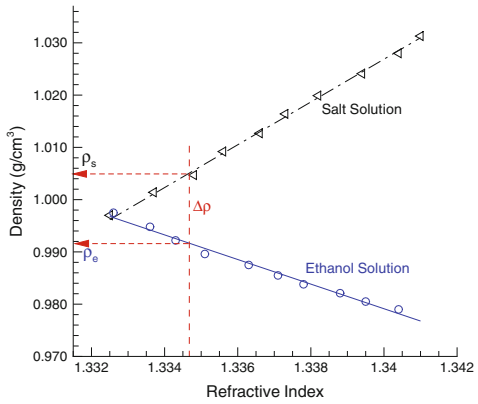

Fig. 4 Densities and refractive indices of ethanol and salt solutions. *Lines* are linearly fitted from the measured data

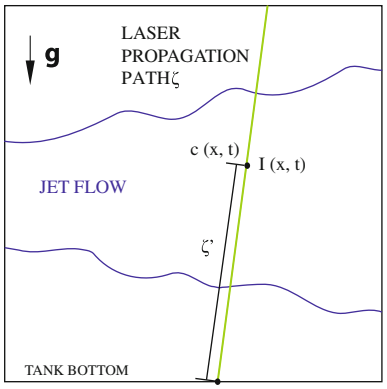

Fig. 5 Schematics of laser propagation in absorbing medium

and 32 × 32 pixels interrogation window and 50% overlap for the second step. A total of 128 × 128 vectors are resolved from each PIV image pair. The sample area of PIV measurement is of 11.0 × 11.0 cm^2, and the spatial resolution is $\Delta = 0.18$ cm (the PIV grid spacing is 0.09 cm). A typical uncertainty estimate of the instantaneous PIV data is about 0.15 pixel, corresponding to an uncertainty of 1%, when estimated using a characteristic velocity of 1.0 m/s and pulse delay of 500 μs. Detail discussions of PIV accuracy analysis can be found in various literatures (e.g., Keane and Adrian 1990; Huang et al. 1997; Chen et al. 2006; Raffel et al. 2007).

3.3 Measuring density field using PLIF

To apply PLIF for measuring concentration (density) field in the present experiment, a fluorescent dye, Rhodamine 6G, is mixed uniformly in the dense fluid. The dye serves as a surrogate of the concentration of dense fluid mixed into light fluid, i.e., the local dye concentration is of a linear relationship with the local density of the mixture. Rhodamine 6G absorbs the excitation light of center around 530 nm and emits fluorescence with a peak at 550 nm (Du et al. 1998). The intensity of the fluorescence is proportional to the dye concentration. Particularly, the same Nd:YAG pulse laser and optics are used to form a laser sheet to excite the fluorescence and to illuminate PIV particles as well (Fig. 3). The PLIF images are recorded by another camera (14-bit Imager ProX 4M CCD camera) with 2,112 × 2,072 pixels resolution.

Grayscale value of every location in the PLIF image g_s is linearly related to the local dye concentration value c and local laser intensity I, i.e.,

$$g_s(\mathbf{x},t) = \Gamma \cdot I(\mathbf{x},t) \cdot c(\mathbf{x},t) + g_b(\mathbf{x}), \tag{5}$$

where constant Γ quantifies the system-specific optical collection efficiency (conversion of photons to digital signals recorded by the CCD sensor) as well as the effective quantum yield of fluorescence dye, and $g_b(\mathbf{x})$ is the background noise. When laser light propagates in the dyed solution, certain portion of laser energy is absorbed by the medium. The laser intensity in this absorbing medium is modeled by Bouguer–Lambert–Beer Law (Fig. 5):

$$I(\mathbf{x},t) = I_o(\mathbf{x}) \cdot \exp\left(-\int_{\zeta} \varepsilon c(\boldsymbol{\zeta}',t) d\boldsymbol{\zeta}' \right), \tag{6}$$

in which $I_o(\mathbf{x})$ is local laser intensity without absorption occurred its path and ε is an extinction coefficient (constant, to-be-determined). $\boldsymbol{\zeta}$ is the laser propagation path in the absorbing medium ($\mathbf{x}_o \rightarrow \mathbf{x}$) and in this experiment it is determined individually by tracing light rays. Thus, Eqs. 5 and 6 lead to

$$g_s(\mathbf{x},t) = \Gamma \cdot I_o(\mathbf{x}) \cdot \exp\left(-\int_{\zeta} \varepsilon c(\boldsymbol{\zeta}',t) d\boldsymbol{\zeta}' \right) \cdot c(\mathbf{x},t) + g_b(\mathbf{x}). \tag{7}$$

One is reminded that $I_o(\mathbf{x})$ is invariant of concentration distribution $c(\mathbf{x}, t)$, whereas $I(\mathbf{x}, t)$ is dependent on $c(\mathbf{x}, t)$.

PLIF calibration. This relationship between local grayscale and dye concentration is quantitatively determined in a calibration procedure, where laser, optics, and camera are set up in an identical way as in the experiments. In the calibration procedure, the main tank is filled with uniformly dissolved dye solution, from 0 to 70 μg/L with a 10 μg/L increment for each of the eight calibration steps. The PLIF camera records a total of 100 fluorescence images of test section for each step. Since the dye concentration is uniform at each calibration step, i.e., $c(\mathbf{x}, t) = c$, from Eq. 7, one has

$$g_s(\mathbf{x}) = \Gamma \cdot I_o(\mathbf{x}) \cdot c \cdot \exp(-\varepsilon c\zeta) + g_b(\mathbf{x}). \quad (8)$$

Since $\varepsilon c\zeta \ll 1$ in the present work, one has $\exp(-\varepsilon c\zeta) \simeq 1 - \varepsilon c\zeta$ from Taylor's expansion. Equation 8 can be rewritten

$$\begin{aligned} g_s(\mathbf{x}) &\simeq \Gamma \cdot I_o(\mathbf{x}) \cdot c \cdot [1 - \varepsilon c\zeta] + g_b(\mathbf{x}) \\ &= [-\Gamma \cdot I_o(\mathbf{x}) \cdot \varepsilon\zeta] \cdot c^2 + [\Gamma \cdot I_o(\mathbf{x})] \cdot c + g_b(\mathbf{x}). \end{aligned} \quad (9)$$

The averaged grayscale values at every pixel location, computed using 100 snapshots at each of the eight calibration concentration levels, are curve fitted to establish a second-order polynomial of concentration c ($g_s(\mathbf{x})$ vs. c, Fig. 6). The obtained polynomial coefficients give local values of $\Gamma \cdot I_o(\mathbf{x})$, $g_b(\mathbf{x})$, and ε. Particularly, in the present experiments, ε is of a measured value of $(1.9 \pm 0.3) \times 10^{-4}$ (cm·μg/L)$^{-1}$.

Mapping of density field. Using the values of $\Gamma \cdot I_o(\mathbf{x})$ and $g_b(\mathbf{x})$ as well as ε obtained from the calibration procedure, the grayscale information of the PLIF images can be converted to concentration of dye solution from Eq. 7

$$c(\mathbf{x}, t) = \frac{g_s(\mathbf{x}, t) - g_b(\mathbf{x})}{\Gamma \cdot I_o(\mathbf{x}) \cdot \left(1 - \int_\zeta \varepsilon c(\boldsymbol{\zeta}', t) d\boldsymbol{\zeta}'\right)}. \quad (10)$$

Furthermore, the density of the jet mixture is

$$\rho(\mathbf{x}, t) = \frac{c(\mathbf{x}, t)}{c_0} \Delta\rho_0 + \rho_e, \quad (11)$$

where c_0 is the initial fluorescence dye concentration in the dense liquid ($c_0 = 60$ μg/L in this study) and $\Delta\rho_0 = \rho_s - \rho_e$ is the initial density difference. The PLIF images are processed using an in-house developed software.

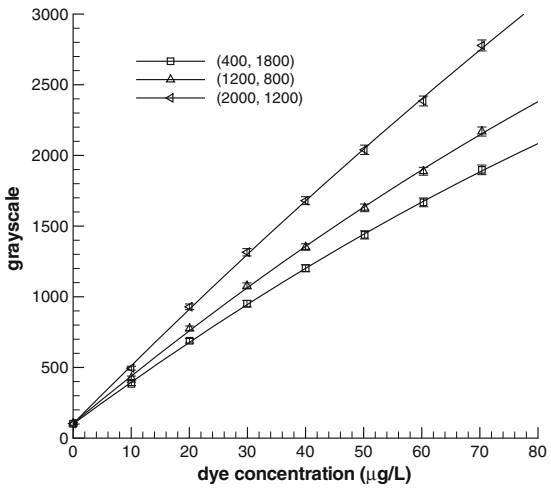

Fig. 6 Characteristic PLIF calibration curves at three characteristic pixel locations in the PLIF image from 100 images at each calibration step. *Symbols* show the ensemble average, and the *error bars* show the rms values

Photobleaching effect and jitter of laser pulse energy. When exposed to excitation illumination for an extended duration, the fluorescence dye may have a reduction in the ability of fluorescence emitting. This photobleaching effect increases uncertainty of PLIF measurement. One may refer to Crimaldi (1997, 2008) and therein references for detailed discussion of photobleaching effects in which illumination using continuous laser is considered. The Nd:YAG pulse laser used in the present study has a pulse width of 8 ns. For a typical run of taking 200 PLIF images, the duration of fluorescence dye being exposed to laser illumination is about 1.2 μs. Since this value is significantly less than that of using continuous laser, the negative influence of photobleaching is expected to be less. However, when pulse laser is used in PLIF measurements, jitter of laser pulse energy may introduce new source of measurement error, i.e., caused by variation of $I_o(\mathbf{x})$ in Eqs. 7 and 10.

In order to quantify the influences of these two factors, we examine the 100 PLIF images recorded consecutively in a calibration run, where the dye concentration is uniform and the flow is still (no replenish of unbleached dye into the illuminated area). Figure 7 shows temporal development of grayscale levels, indicating the emitted fluorescence level, at three characteristic pixel locations in a calibration image sequence where dye concentration is 70 μg/L. The grayscale of the recorded PLIF calibration image is a function of laser intensity and characteristics of imaging system (including white noise of CCD). Therefore, the variations in the sequences of each location in Fig. 7 are caused by both variation of laser intensity and white noise of CCD. In other words, the local fluctuation on these curves can be attributed to both the laser jittering and the noise generated by the imaging system, whereas photobleaching may introduce a systemically decreased trend, if there is any. However, the data do not show such a decreasing trend of $g_s(\mathbf{x})$ as N (or time t) increases in Fig. 7. This suggests that, because of the use of pulse laser with a narrow pulse width, the photobleaching effect is neglectable during the data acquisition process in the present study. At the three locations, A, B, and C, the rms values of grayscale levels are 18, 15, and 16, respectively. Compared to their corresponding mean values, these rms fluctuations are of relative levels of 0.8, 1, and 0.6%, respectively.

Uncertainty of density measurement. To estimate the uncertainty of PLIF measurement, the laser intensity attenuation through the test section is ignored for the time being. From Eqs. 10 and 11, one has

$$\Delta\rho(\mathbf{x}, t) = \frac{g_s(\mathbf{x}, t) - g_b(\mathbf{x})}{\Gamma \cdot I_o(\mathbf{x})} \cdot \frac{\Delta\rho_0}{c_0}. \quad (12)$$

Then, there are four sources making contributions to the uncertainty of the instantaneous density measurement, i.e.,

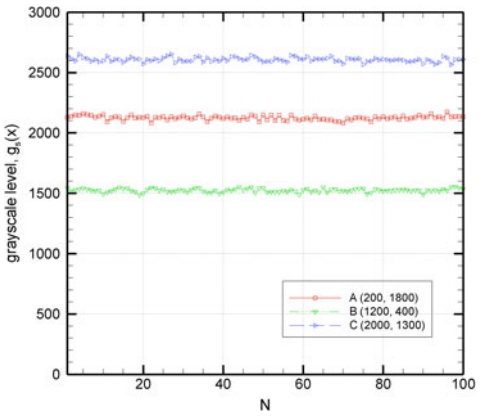

Fig. 7 Grayscale levels in 100 consecutively recorded PLIF calibration images at three pixel locations. *Horizontal axis* is the image index ($N = 1, 2, \ldots, 100$), and the lines give averaged values using the 100 samples

$$\Delta\rho = f(g_s, \Gamma I_o, \Delta\rho_0, c_0). \tag{13}$$

The uncertainty of density measurement can be analyzed from the error propagation. At a characteristic pixel location (1,200, 400), corresponding to curve B (lowest of the three) in Fig. 7, and characteristic dye concentration $c_0 = 60$ μg/L in the PLIF measurement, the four uncertainty sources are: uncertainty of $g_s \sim 1.69$ (determined from background images without dye), uncertainty of $(\Gamma \cdot I_o) \sim 0.8072$ L/μg, uncertainty of $\rho_0 \sim 0.5$ g/L, and uncertainty of $c_0 \sim 0.015$ μg/L. The relative uncertainty of instantaneous density measurement at this characteristic location is about 2%. The uncertainties at other locations are smaller or close to this characteristic value. One is reminded that the uncertainty analysis presented here uses the results from a static calibration process (recording PLIF images from a tank filled with uniformly dyed solution, as described in Sect. 3.3). In the experiments, the dye concentration is a dynamic function of time and space. This suggests that the uncertainty could be underestimated from the static calibration process. More research is needed to develop an advanced dynamic calibration procedure for PLIF experiments.

3.4 Simultaneous density–velocity measurement

To measure the density and velocity fields simultaneously, we combine the PIV and PLIF system (Fig. 3). A PIV filter (bandpass, center wavelength 530 ± 10 nm) is mounted on the PIV camera to pass the scatter light from PIV particles and block the fluorescence signal. A PLIF filter (longpass with cutoff 550 nm) is used to block the PIV signal and pass the fluorescence signal only. Cameras and laser are synchronized by a pulse generator so that both cameras take images of test section in a simultaneous way. Different than another two-camera setup described in Chen et al. (2007) and Odier et al. (2009), where a beam splitter splits the image signal from test section toward two cameras at a 50%/50% ratio, a scheimpflug lens mount is used on the PLIF camera to keep the PLIF image focused when the camera points to the test section at a tilt angle $\alpha \sim 15°$). This arrangement eliminates the 50% signal loss due to use of a beam splitter. The sample area of PLIF camera encloses the sample area of PIV camera, so that the PLIF image can be subsampled to obtain the concentration field over the entire 128 × 128 PIV grid. For every grid node, there is a velocity vector measured from PIV and a corresponding density value from PLIF.

4 Experimental conditions

We conduct measurements within the central vertical plane ($y = 0$, Fig. 1) at three consecutive downstream locations (along the x direction, labeled as P1–P3 in Fig. 3). At each location, a total of 600–2,000 snapshots are recorded, from multiple runs, to form an ensemble set for statistical analysis. During the effective measurement period of each run, the height change of the free surface is ignorable. After each run, the main tank is drained and rinsed to remove the residual fluorescence dye. Then, the liquids in both tanks are prepared again for next run.

In addition to measurements of stratified jet at two different sets of conditions, as summarized in Table 1, we also measure the velocity fields of unstratified jet (no density difference, thus no PLIF measurement). Among the four cases, we refer to case 2 as "low-*Ri*" case ($Ri_0 = 0.0002$) and case 4 as "high-*Ri*" case ($Ri_0 = 0.01$). The two unstratified cases are indicated by "high-*Re*" ($Re = 24{,}000$) case and "low-*Re*" case ($Re = 3{,}200$).

5 Results

A typical snapshot of velocity and density fields is shown in Fig. 8, in which the jet structure and dilution of dense fluid can be identified. As the jet flow moves downstream, complex mixing and entrainment structures are visualized from the measured results.

5.1 Mean parameters and structures of stratified jet

The ensemble averaged velocity component $\langle U_1 \rangle$, vorticity component $\langle \Omega_2 \rangle$, and nondimensional density difference $\langle \theta \rangle$ are shown in Figs. 9 and 10, where the data from consective frames are plotted together. In low-*Ri* case (Fig. 9), the z-locations of the peak velocity in the profiles

Table 1 Summary of parameters at the jet exit ($x/D = 0$)

Case	1 "High-*Re*"	2 "Low-*Ri*"	3 "Low-*Re*"	4 "High-*Ri*"
Jet velocity (mean) U_0 (m/s)	1.88	1.88	0.24	0.24
Jet velocity fluctuation (rms) u (m/s)	0.062	0.113	0.008	0.008
Turbulence intensity $I = u/U_0$	3.3%	6.0%	3.4%	3.5%
Initial density difference $\Delta\rho_0/\rho_s$	0	0.5%	0	0.5%
Reynolds number $Re_0 = \rho_s U_0\, D/\mu$	24,000	24,000	3,200	3,200
Richardson number $Ri_0 = \Delta\rho_0 Dg/(\rho_s {U_0}^2)$	0	0.0002	0	0.01
Estimated dissipation rate $\epsilon = u^3/D\,(\mathrm{m}^2/\mathrm{s}^3)$	0.019	0.11	0.00004	0.00004
Kolmogorov scale $\eta_K = (\nu^3/\epsilon)^{1/4}$ (mm)	0.09	0.05	0.40	0.38
Bathelor lengthscale $\eta_B = (\nu\kappa^2/\epsilon)^{1/4}$ (mm)	0.0009	0.0006	0.004	0.004
(PIV spatial resolution Δ)/η_K	20	36	4.5	4.7

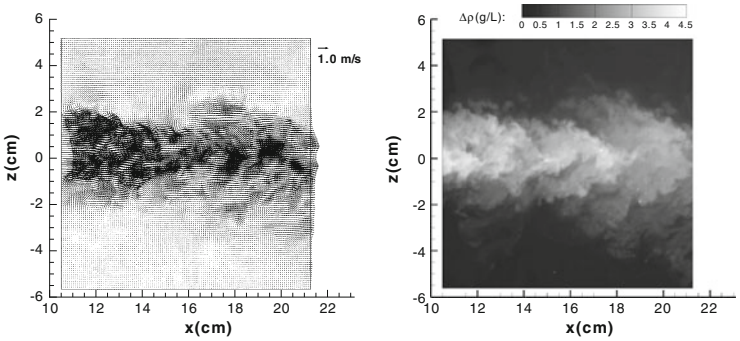

Fig. 8 A snapshot of simultaneous velocity (*left*) and density (*right*) fields of low-*Ri* case

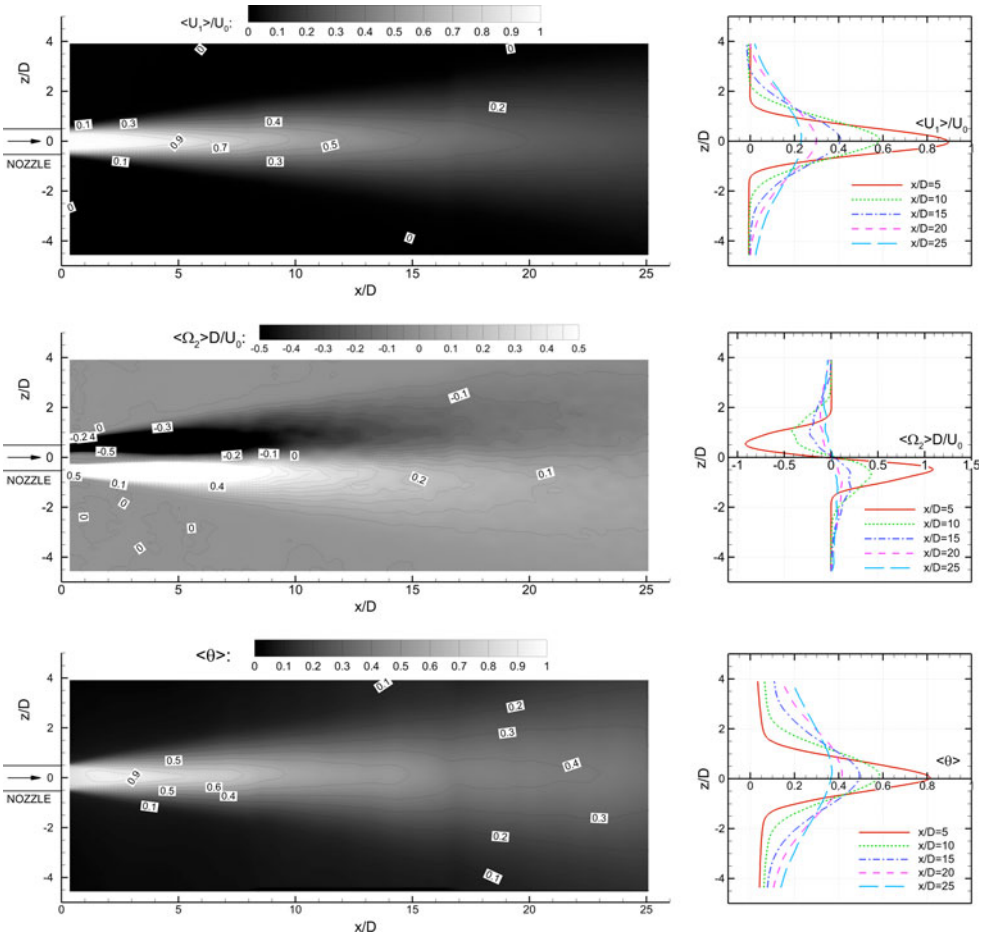

Fig. 9 Development of (*top*) the mean velocity component $\langle U_1 \rangle$, (*middle*) vorticity component $\langle \Omega_2 \rangle$, and (*bottom*) the mean non-dimensional density $\langle \theta \rangle$ showing the mean flow pattern of the low-*Ri* case. *Right plots* show the corresponding z-profiles

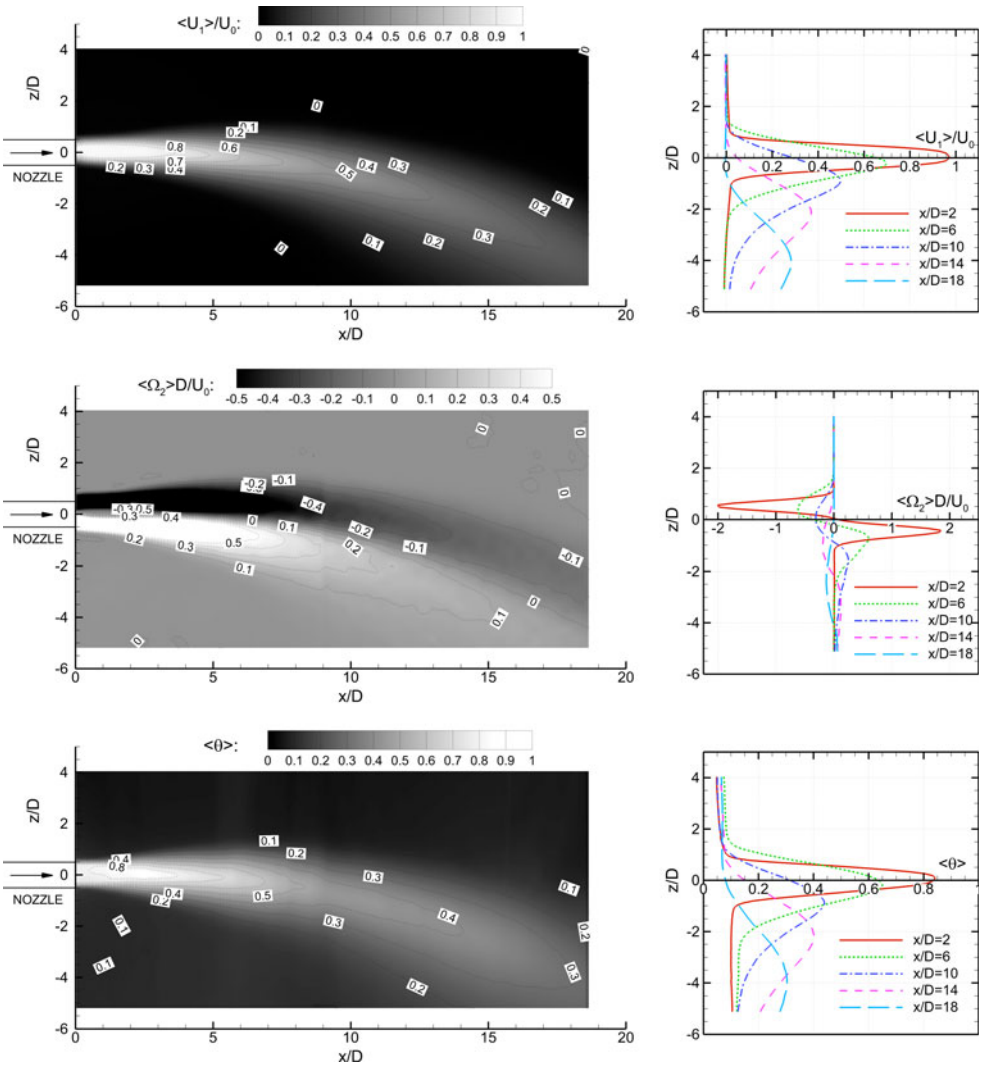

Fig. 10 Development of (*top*) the mean velocity component $\langle U_1 \rangle$, (*middle*) vorticity component $\langle \Omega_y \rangle$, and (*bottom*) the mean non-dimensional density $\langle \theta \rangle$ showing the mean flow pattern of the high-*Ri* case. *Right plots* show the corresponding z-profiles

deviate from $z = 0$ slightly (one is reminded that for unstratified jet the velocity profiles always peak at $z = 0$ due to symmetry). The magnitude of the peak velocity decreases along the main flow (x) direction, whereas the span of the jet structure increases. Density profiles in Fig. 9 have similar trend as those of velocity profiles, but spread wider. Strong vortices are generated near the nozzle exit, and their magnitude decreases along x direction. In high-*Ri* case (Fig. 10), the magnitude of the peak velocity decreases as jet expands along x direction. The location of peak velocity in profiles significantly deviates from $z = 0$ as flow moves to downstream. The expansion of velocity profiles in stable stratification region is less than that in unstable stratification region, and the similar phenomenon is observed from density profiles.

To characterize the deviation of velocity peak from $z = 0$, a z_o^2 is defined, to indicate center of the stratified jet, such that $U_c(x) \equiv \langle U_1 \rangle (x, 0, z_c^u)$ where $U_c(x)$ is the peak velocity (x-component). The corresponding z-component of mean velocity at the same location is $W_c(x) \equiv \langle U_3 \rangle (x, 0, z_c^u)$. Previous experiments on unstratifed jet, as summarized in Pope (2001), show that the inverse of $U_c(x)$ is proportional to x, i.e.,

$$\frac{U_c(x)}{U_0} = \frac{B}{(x - x_o)/D}, \tag{14}$$

where B is an empirical velocity-decay constant and x_o is a virtual origin. Figure 11 shows the development of $U_0/U_c(x)$ as a function of x/D for all four cases in the present study. $U_c(x)$ seems insensitive to the stratification, i.e., it displays the same decay rate $B = 0.58$ in low-*Ri* case and unstratified high-*Re* case ($Re = 24{,}000$ in both cases). $B = 0.63$ is obtained in the high-*Ri* case and unstratified low-*Re* case ($Re = 3{,}200$ in both cases). One may conclude that B is dependent on *Re* only for stratified jets. The development of $W_c(x)$ is of strong *Ri*-dependence, as shown in Fig. 11.

The center of the stratified jet, z_c^u, can be best described by a second-order polynomial, i.e.,

$$z_c^u(x)/D \simeq -\beta(x/D)^2, \tag{15}$$

in which β describes the extent of the deviation. The *Ri*-dependence of β is quantified using our experiment data, as shown in Fig. 12. This trend is consistent with the fact that when $Ri \to \infty$ we expect $\beta \to \infty$, as in vertical plumes. From Eq. 15, this leads to:

$$z_c^u(x)/D \simeq -0.2\sqrt{Ri_0} \cdot (x/D)^2. \tag{16}$$

To study the expansion of the jet, we examine locations of the jet velocity profiles in stably stratification region, $z^u_{+1/2}$, and unstably stratification region, $z^u_{-1/2}$, where x velocity component reaches half of $U_c(x)$, i.e.,

$$\langle U_1\rangle(x,0,z^u_{+1/2}) = \langle U_1\rangle(x,0,-z^u_{-1/2}) = 1/2U_c(x). \tag{17}$$

Moreover, the characteristic velocity half-widthes, $r^u_{\pm 1/2}$, are defined as

$$r^u_{+1/2} = z^u_{+1/2} - z^u_c, \quad r^u_{-1/2} = -z^u_{-1/2} + z^u_c. \tag{18}$$

Similarly, the density half-width locations of the jet, $z^\theta_{+1/2}$ and $z^\theta_{-1/2}$, are defined such that

$$\langle\theta(x,0,z^\theta_{+1/2})\rangle = \langle\theta(x,0,-z^\theta_{-1/2})\rangle = 1/2\theta_c(x), \tag{19}$$

where $\theta_c(x)$ is the peak density. The density half-widthes are

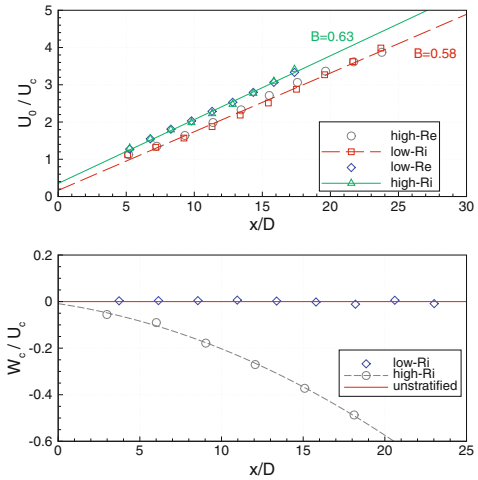

Fig. 11 Downstream developments of (*top*) U_0/U_c and (*bottom*) W_c/U_c

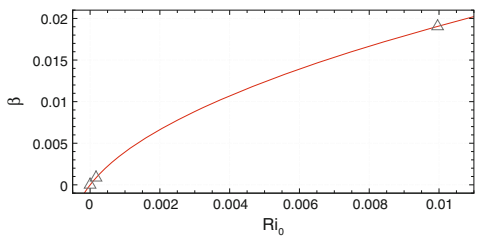

Fig. 12 Dependence of coefficient β on Richardson number Ri_0

$$r^\theta_{+1/2} = z^\theta_{+1/2} - z^\theta_c, \quad r^\theta_{-1/2} = -z^\theta_{-1/2} + z^\theta_c, \tag{20}$$

where z^θ_c is the peak density location. The measurement data indicate that z^u_c and z^θ_c are nearly coincident, so we denote $z_c = z^u_c \simeq z^\theta_c$. Downstream developments of $r^u_{\pm 1/2}$ and $r^\theta_{\pm 1/2}$ are shown in Fig. 13. In low-*Ri* case, one may observe $r^u_{+1/2} \simeq r^u_{-1/2} \simeq r^u_{1/2}$, while $r^\theta_{+1/2}$ and $r^\theta_{-1/2}$ are also nearly coincident, but the density curves are larger than velocity curves. However, in high-*Ri* case, further comparisons with unstratified low-*Re* case show that $r^u_{-1/2} > r^u_{+1/2} \simeq r^\theta_{1/2}$. From this figure, one can observe that as *Ri* increases the stratified jet expands more asymmetrically as it moves to downstream and $r^u_{+1/2}$ can be always approximately described by its unstratified counterpart $r^u_{1/2}$.

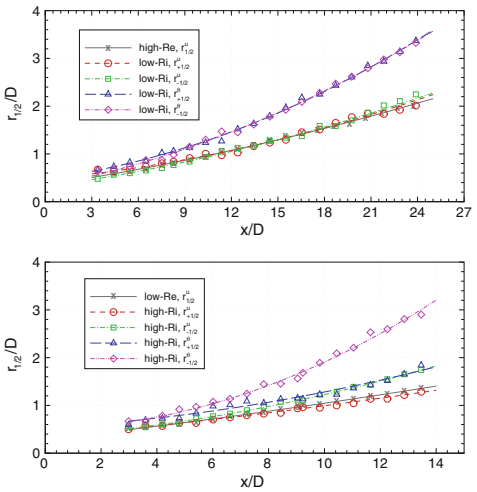

Fig. 13 Development of the halfwidthes of stratified jet: (*top*) low-*Ri* case and (*bottom*) high-*Ri* cases

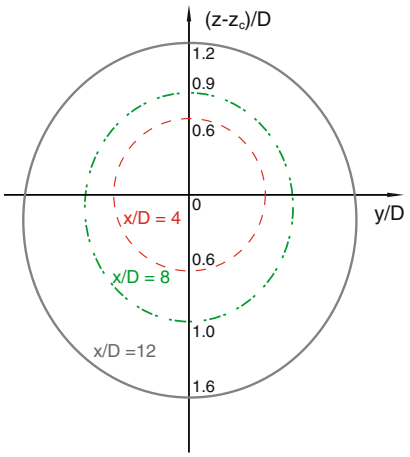

Fig. 14 Qualitative illustration of jet profiles (defined by the velocity half-width) at different downstream locations

In the unstable stratification region, turbulent mixing is enhanced by stratification and thus momentum and density diffuse significantly faster than in the stable stratification region. Figure 14 depicts $y-z$ profiles of the velocity half-widthes for the high-*Ri* case at three downstream locations (where the y-intercepts of the profiles are qualitatively estimated by averaging $r^{u}_{+1/2}$ and $r^{u}_{-1/2}$). At $x/D = 4$, the profile is nearly circle because the inertial effect is dominant near nozzle exit, while the profiles at downstream locations $x/D = 8$ and 12 deform into ellipse shape because of the two different stratification mechanisms. The different effects of stable and unstable stratifications are also reflected in the similarity profiles, as shown in Fig. 15. As bulk Richardson number increases, the profiles gradually deviate from the nearly universal similarity profiles owned by unstratifed cases (turbulent jets). In the upper region ($z - z_c > 0$), the expansion of the jet profile is less than that of unstratified jet due to crippled mixing. In the lower region ($z - z_c < 0$), on the contrary, the expansion of the jet profile is larger due to enhanced mixing from unstable stratification. The observed deviation in these profiles (Fig. 15) also reveals the inadequacy of applying similarity analysis to stratified flows using velocity data. The influence of Richardson number, as well as the different effects of stable and unstable stratification, should be accounted.

5.2 Reynolds stress and vertical density flux

The profiles of $-\rho\langle u_1 u_3\rangle$ and $g'\langle\theta' u_3\rangle$ at different downstream locations are shown in Fig. 16 for both low-*Ri* and high-*Ri* cases. For low-*Ri* case where buoyancy effect is not significant, these profiles are nearly antisymmetric with respect to $z/D = 0$. However, for high-*Ri* case, these profiles deviate from antisymmetry as x/D increases, because of different roles of stable stratification and unstable stratification. In addition, in high-*Ri* case, the peaks of $-\rho\langle u_1 u_3\rangle$ and $g'\langle\theta' u_3\rangle$ in the stable stratification region decrease faster than those in the unstable stratification region. These profiles also demonstrate a strong correlation between $-\rho\langle u_1 u_3\rangle$ and $g'\langle\theta' u_3\rangle$ in both low-*Ri* and high-*Ri* cases at different downstream locations.

5.3 Energetics of stratified jet

In stratified flows, the transport equation of turbulent kinetic energy (TKE), $k = \langle u_i u_i\rangle/2$, is: (e.g., Turner 1973)

$$\langle U_j\rangle\frac{\partial k}{\partial x_j} + \frac{\partial T_j}{\partial x_j} = \mathcal{P} - \mathcal{B} - \epsilon, \tag{21}$$

where

$$T_j = \frac{1}{2}\langle u_j u_i u_i\rangle + \frac{1}{\rho_s}\langle u_j p\rangle - 2\nu\langle u_i s_{ij}\rangle. \tag{22}$$

TKE is computed here using,

$$k = \frac{1}{2}(\langle u_1^2\rangle + \langle u_2^2\rangle + \langle u_3^2\rangle) \simeq \frac{1}{2}(\langle u_1^2\rangle + 2\langle u_3^2\rangle), \tag{23}$$

i.e., with the assumption of $\langle u_2^2\rangle \simeq \langle u_3^2\rangle$. For clarity, we denote turbulence transport and mean-flow convection terms on the left-hand side of Eq. 21 as

$$\Phi = \langle U_j\rangle\frac{\partial k}{\partial x_j}, \quad \Psi = \frac{\partial T_j}{\partial x_j}. \tag{24}$$

The turbulence production $\mathcal{P}$ represents the production (source) mechanisms of TKE and thus quantifies the energy transfer from large-scale mean flow to small-scale turbulence:

$$\mathcal{P} = -\langle u_i u_j\rangle S_{ij} \quad \text{where} \quad S_{ij} = \frac{1}{2}\left(\frac{\partial\langle U_i\rangle}{\partial x_j} + \frac{\partial\langle U_j\rangle}{\partial x_i}\right). \tag{25}$$

The buoyancy flux $\mathcal{B}$ quantifies the TKE production or destruction via mixing caused by irreversible destruction of local density gradients to produce a vertical mass flux

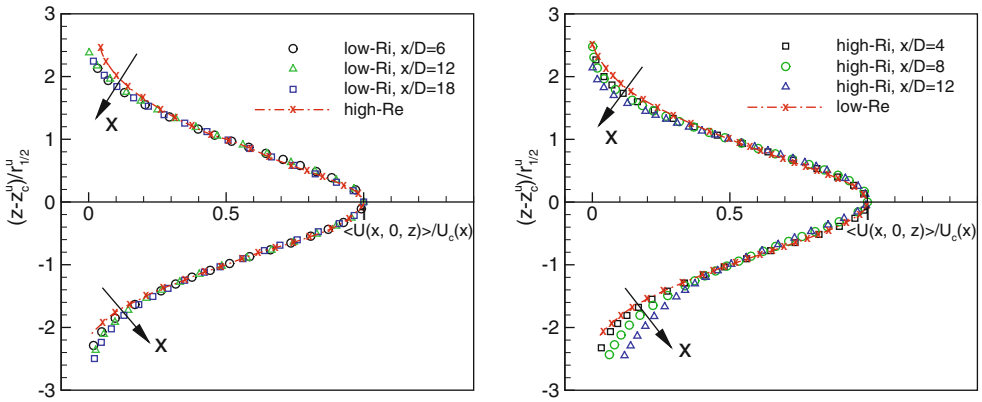

Fig. 15 Velocity similarity profiles at different downstream locations and comparison with unstratified jet results. (*Left*) low-*Ri* case and (*right*) high-*Ri* case

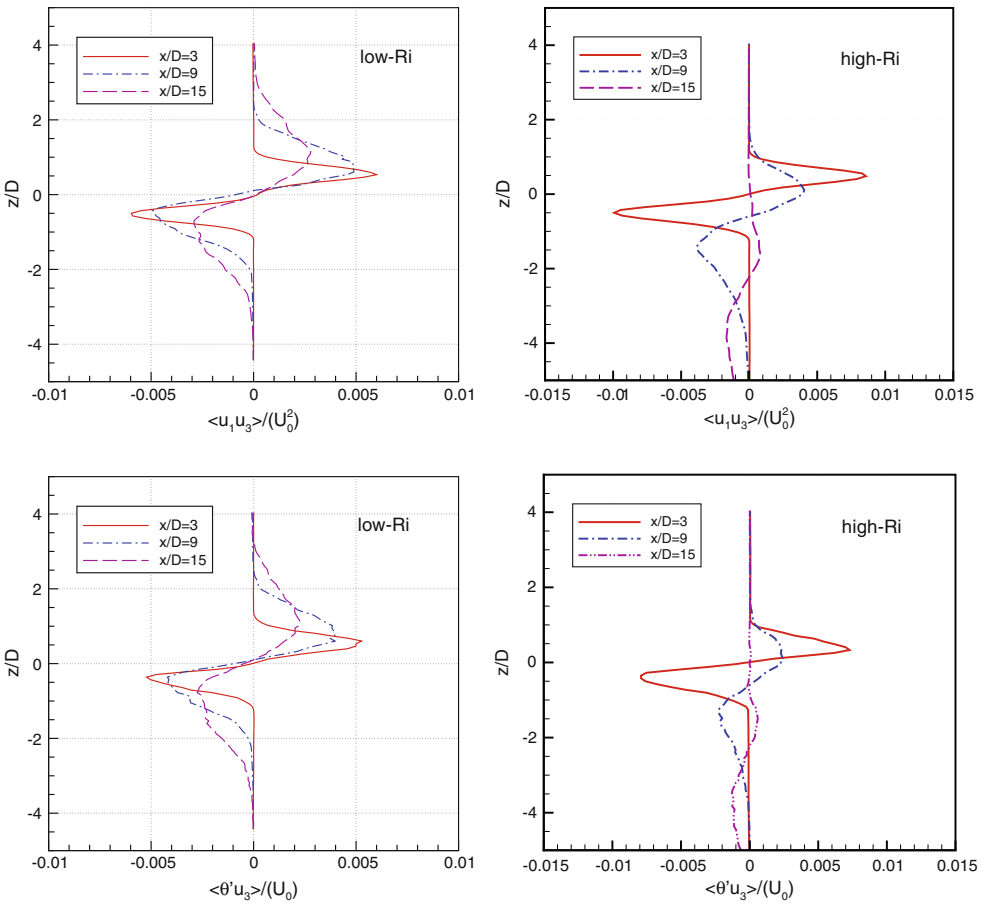

Fig. 16 Development of $\langle u_1 u_3 \rangle$ and $\langle \theta' u_3 \rangle$ at different downstream locations ($x/D = 3$, 9, 15) in (*left*) low-*Ri* and (*right*) high-*Ri* cases

$$\mathcal{B} = g' \langle \theta' u_3 \rangle. \tag{26}$$

The last term of Eq. 21,

$$\epsilon = \nu \left\{ \left\langle \frac{\partial u_i}{\partial x_j} \frac{\partial u_i}{\partial x_j} \right\rangle + \left\langle \frac{\partial u_i}{\partial x_j} \frac{\partial u_j}{\partial x_i} \right\rangle \right\}, \tag{27}$$

represents the dissipation (sink) mechanism of TKE by viscous stresses. Using the measured velocity and density data, development of turbulent production, buoyancy flux, and dissipation are calculated using the Eqs. 25, 26, and 27. Particularly, in our study, $\langle U_2 \rangle = 0$ in our measurement plane ($x_2 = 0$), due to symmetry of mean flow, which leads to $\partial \langle U_2 \rangle / \partial x_1 = 0$ and $\partial \langle U_2 \rangle / \partial x_3 = 0$. In addition, this symmetry gives $\partial \langle U_i \rangle / \partial x_2 = 0 (i = 1, 2, 3)$. Therefore, $\mathcal{P}$ can be directly calculated using all resolved terms from PIV measurements, i.e.,

$$\mathcal{P} = -\langle u_1^2 \rangle \frac{\partial \langle U_1 \rangle}{\partial x_1} - \langle u_1 u_3 \rangle \frac{\partial \langle U_1 \rangle}{\partial x_3} - \langle u_1 u_3 \rangle \frac{\partial \langle U_3 \rangle}{\partial x_1} - \langle u_3^2 \rangle \frac{\partial \langle U_3 \rangle}{\partial x_3}. \tag{28}$$

ϵ is estimated by the resolved terms, i.e.,

$$\epsilon \simeq \left\langle 4 \left(\frac{\partial u_1}{\partial x_1} \right)^2 + 4 \left(\frac{\partial u_3}{\partial x_3} \right)^2 + 4 \frac{\partial u_1}{\partial x_1} \frac{\partial u_3}{\partial x_3} + 3 \left(\frac{\partial u_1}{\partial x_3} \right)^2 + 3 \left(\frac{\partial u_3}{\partial x_1} \right)^2 + 6 \frac{\partial u_1}{\partial x_3} \frac{\partial u_3}{\partial x_1} \right\rangle, \tag{29}$$

where the unresolved terms are expressed by a local isotropy assumption (see details in Doron et al. 2001). One is reminded that the direct estimation of ϵ using PIV data can be relatively qualitative, particularly for low-*Ri* case where the measurement resolution is not close to the turbulent Kolmogorov scale. Extended discussion of analyzing ϵ using PIV data and associated uncertainty analysis can be found in, e.g., Doron et al. (2001), Chen et al. (2006), and de Jong et al. (2009). In addition, we estimate the mean-flow convection term, i.e.,

$$\Psi = \mathcal{P} - \epsilon - \mathcal{B} - \Phi. \tag{30}$$

As shown in Fig. 17, the profiles of energy budget terms are nearly symmetric with respect to $z/D = 0$ near nozzle exit ($x/D = 3$), but deviate from symmetry at further downstream. One is reminded that the profiles of these terms in unstratified case ($Ri = 0$) are symmetric at all

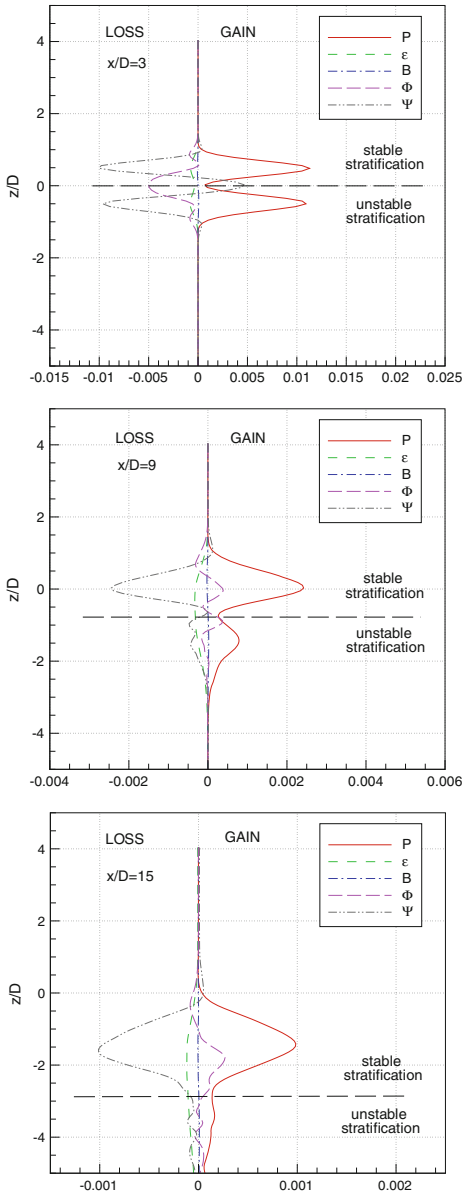

Fig. 17 Energy budget terms $(-\Phi, -\Psi, \mathcal{P}, -\mathcal{B}, -\epsilon)$ in high-*Ri* case at three downstream locations ($x/D = 3$, 9, 15). One is reminded that the range of *horizontal axes* is different for clarity of display, and $\Psi = \mathcal{P} - \epsilon - \mathcal{B} - \Phi$ (Eq. 30)

downstream locations. The magnitude of $\mathcal{B}$ is significantly less than those of $\mathcal{P}$ and ϵ (e.g, $B/P \simeq 1\%$ at $x/D = 3$ and $z/D = 0.06$). Careful examination of $\mathcal{B}$ reveals that $\mathcal{B} > 0$ in the stable stratification region, whereas in the unstable stratification region $\mathcal{B} < 0$. At $x/D = 3, \mathcal{P}$ has two balanced peaks. As x/D increases, the peak of $\mathcal{P}$ in stable stratification region overweighs the peak in unstable stratification region, and latter disappears at further downstream (e.g. $x/D = 15$). At $x/D = 3, \Psi$ nearly balances $\mathcal{P}$ in both stable and unstable stratification regions, and this trend remains in the stable stratification

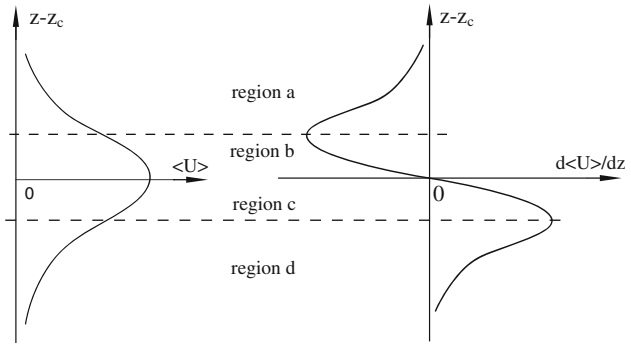

Fig. 18 Division of the jet flow into 4 regions (*a*, *b*, *c*, and *d*) along *z* direction

region at $x/D = 15$. However, Ψ nearly balances Φ in the unstable stratification region at $x/D = 15$. At $x/D = 3, \mathcal{P} - \Psi - \Phi \simeq 0$ in the developing core region of the jet $(-0.5 < z/D < 0.5)$, and $\Phi + \Psi \simeq 0$ in the unstable stratification region at $x/D = 15$. Furthermore, ϵ is small compared to $\mathcal{P}$ in the stable stratification regions at all measured downstream locations, but $\epsilon \simeq \mathcal{P}$ in the unstable stratification region at $x/D = 15$, where the fluid is well mixed.

5.4 Eddy viscosity and eddy diffusivity

The simultaneous velocity–density measurements in the present study enable us to analyze the model coefficients in eddy viscosity type turbulent models for effective simulation of stratified flows, i.e., from Eqs. 3 and 4,

$$\kappa_v = -\frac{\langle u_1 u_3 \rangle}{\partial \langle U_1 \rangle / \partial x_3}, \kappa_\rho = -\frac{\langle \theta' u_3 \rangle}{\partial \langle \theta \rangle / \partial x_3}. \tag{31}$$

Odier et al. (2009) report that the turbulent transport of momentum and density in a gravity current can be effectively described in a direct and compact form by a Prandtl mixing model (e.g., Hinze 1987):

$$\langle u_1 u_3 \rangle = -\mathcal{L}_v^2 \frac{\partial \langle U_1 \rangle}{\partial x_3} \left| \frac{\partial \langle U_1 \rangle}{\partial x_3} \right|, \tag{32}$$

$$\langle \theta' u_3 \rangle = -\mathcal{L}_\rho^2 \frac{\partial \langle \theta \rangle}{\partial x_3} \left| \frac{\partial \langle U_1 \rangle}{\partial x_3} \right|, \tag{33}$$

in which $\mathcal{L}_\rho$ and $\mathcal{L}_v$ are momentum and density mixing lengths. The results of the stably stratified gravity support that $\mathcal{L}_\rho = \mathcal{L}_v$. Further comparison shows that the mixing length description does not work well in unstratified results, suggesting that stratification plays a key role in correlating the flux terms to the mean gradient terms (Odier et al. 2009).

To characterize the effective modeling of vertical flux terms $\langle u_1 u_3 \rangle$ and $\langle \theta' u_3 \rangle$, the flow field is discomposed into four regions (a to d, Fig. 18), based on values of mean

velocity gradient $\partial\langle U_1\rangle/\partial x_3$. Regions a and b (in the stable stratification domain) indicate mixing layer and the core of jet, respectively. Regions c and d (in unstable stratification region) indicate the core of jet and mixing layer, respectively. We explore the relationships between $\langle u_1 u_3\rangle$ and $\partial\langle U_1\rangle/\partial x_3$ and between $\langle \theta' u_3\rangle$ and $\partial\langle\theta\rangle/\partial x_3$ in these four regions, as shown in Figs. 19 and 20. The following observations are made: (1) In the unstratified jet (low-*Re* case), in regions a and d (active mixing with ambient fluid), $\langle u_1 u_3\rangle$ and $\partial\langle U_1\rangle/\partial x_3|\partial\langle U_1\rangle/\partial x_3|$ are of nearly linear relationship, which indicates a suitable application of mixing length model in these regions. In regions b and c (core of the jet), however, $\langle u_1 u_3\rangle$ and $\partial\langle U_1\rangle/\partial x_3$ are of linear relationship and thus the eddy viscosity model (with a constant value of κ_ρ at a given downstream location) performs better. (2) Similar trends are observed in the upstream locations of stratified high-*Ri* case, where the turbulence effect is dominant (as in the unstratified case). As moving to downstream, however, region a, where the stable stratification and active mixing are both present, demonstrates a better performance of mixing length model for modeling $\langle u_1 u_3\rangle$, whereas $\langle u_1 u_3\rangle$ in regions b–d is better modeled by eddy viscosity model. (3) A same conclusion on $\langle \theta' u_3\rangle$ can be drawn for the stratified high-*Ri* case, where the buoyancy effect becomes significant after a certain downstream location (Fig. 20). (4) The low-*Ri* case shows a consistent trend in both reported downstream locations: better performances of eddy viscosity model in regions b and c and mixing length model in regions a and d. This can be explained by the fact in low-*Ri* case the turbulence effect still overweighs buoyancy effect at $x/D = 12$. We conjecture at far enough downstream locations (turbulence effect decays significantly) the same phenomena will be observed as in the high-*Ri* case where mixing length model works better only in the stable stratification region. A conclusion can also be drawn that turbulence models ($\langle u_1 u_3\rangle$ and $\langle \theta' u_3\rangle$) should be treated separately in stable stratification and unstable stratification regions. This discovery further elaborates the one observed by Odier et al. (2009) in a 2D gravity current.

Furthermore, the downstream developments of κ_ν and κ_ρ are analyzed using Eq. 31, as shown in Fig. 21. For the unstratified cases and stratified low-*Ri* case, where the buoyancy effect is absent or weak, κ_ν and κ_ρ keeps on increasing as x increases. In the high-*Ri* case, however, their values indicate a slight increase at upstream, followed by a decrease. The development of mixing lengths, $\mathcal{L}_\nu$ and $\mathcal{L}_\rho$, is also analyzed using data from region a, as shown in Fig. 22. It is observed that $\mathcal{L}_\nu \simeq \mathcal{L}_\rho$ in both stratified cases. Also as *Ri* increases, $\mathcal{L}_\nu$ and $\mathcal{L}_\rho$ stop to increase as a

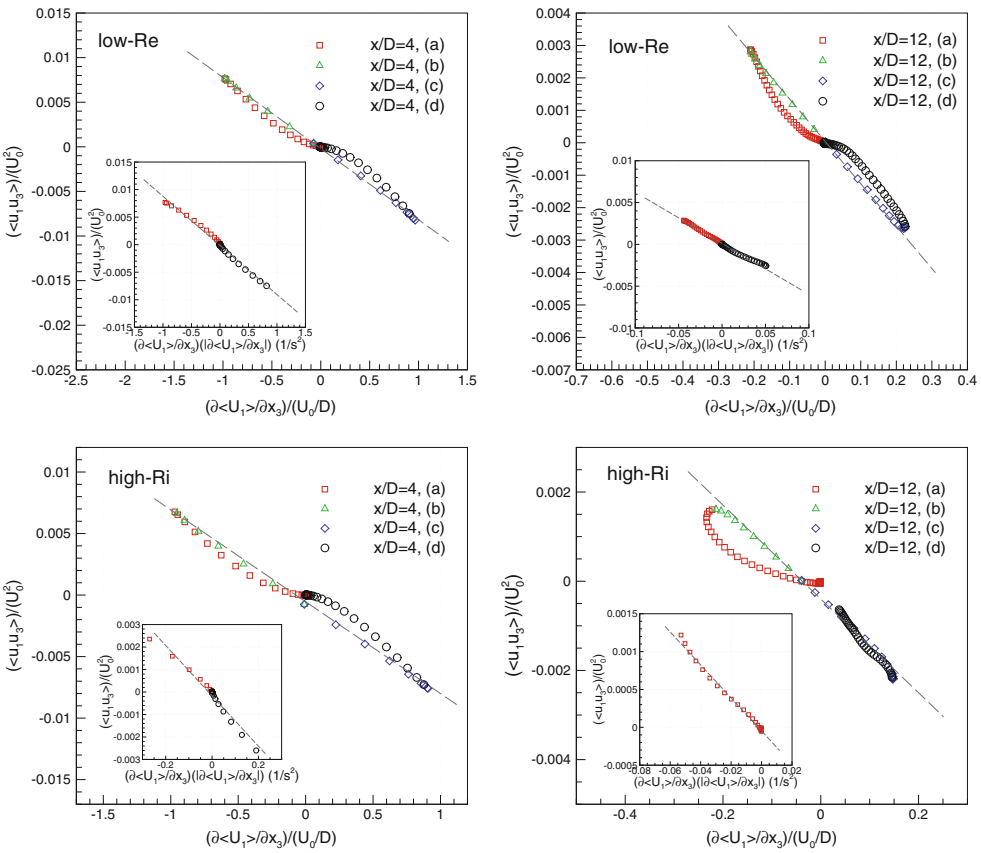

Fig. 19 Scatter plots relate turbulent shear stress ($\langle u_1 u_3\rangle$) and mean velocity gradient ($\partial\langle U_1\rangle/\partial x_3$) at two characteristic x locations (upstream: $x/D = 4$, and downstream: $x/D = 12$). *Insets* show $\langle u_1 u_3\rangle$ versus $\partial\langle U_1\rangle/\partial x_3|\partial\langle U_1\rangle/\partial x_3|$. *Top* unstratified low-*Re* case. *Bottom* high-*Ri* case. The aspect ratios between *horizontal* and *vertical* axes in all plots are the same for direct comparison of slopes. *Dash lines* show the best linear curve fit

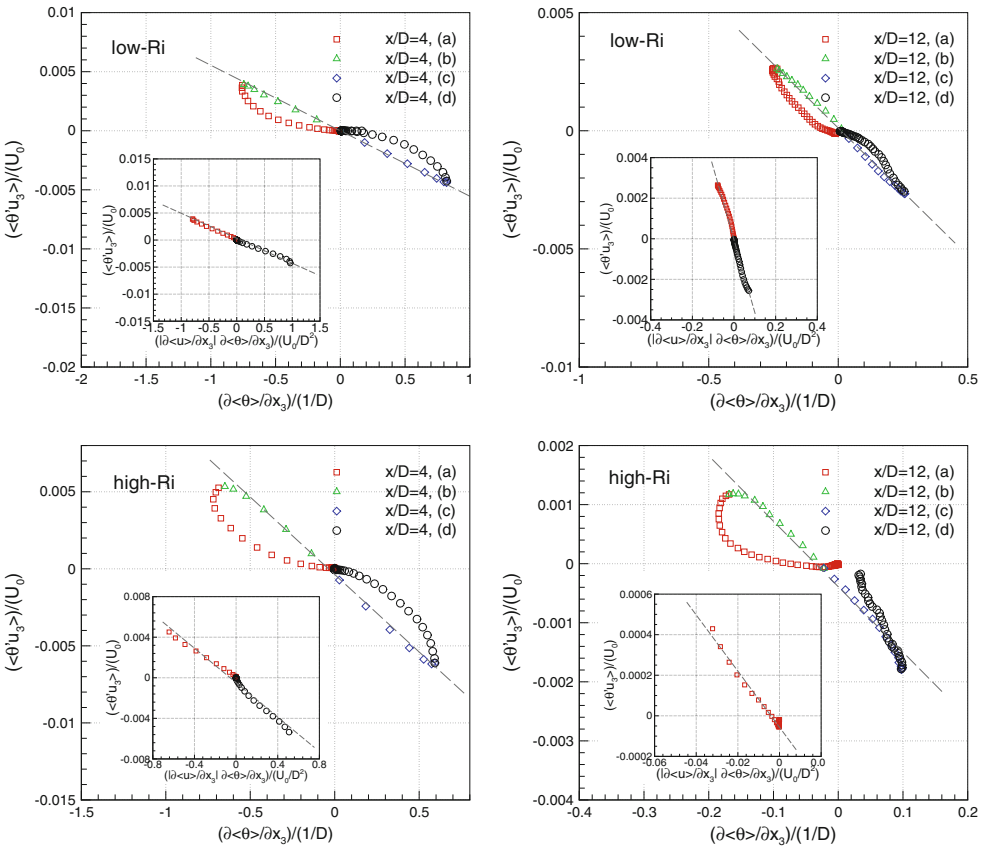

Fig. 20 Scatter plots relate density flux ($\langle\theta' u_3\rangle$) and mean density gradient ($\partial\langle\theta\rangle/\partial x_3$) at two characteristic x locations (upstream: $x/D = 4$, and downstream: $x/D = 12$). *Insets* show $\langle\theta' u_3\rangle$ versus $\partial\langle\theta\rangle/\partial x_3|\partial\langle U_1\rangle/\partial x_3|$. *Top* low-*Ri* case. *Bottom* high-*Ri* case. The aspect ratios between horizontal and vertical axes in all plots are the same for direct comparison of slopes. *Dash lines* show the best linear curve fit

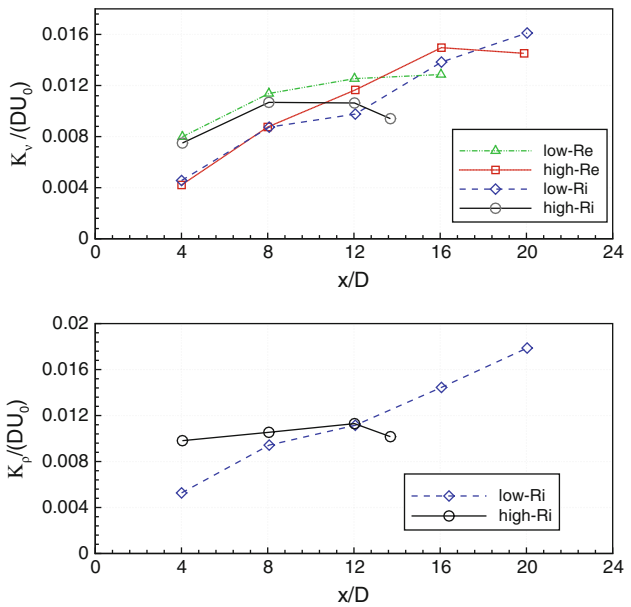

Fig. 21 Development of (*top*) κ_v and (*bottom*) κ_ρ at different downstream locations

function of x. In addition, turbulent Prandtl number is calculated:

$$Pr_T = \frac{\kappa_v}{\kappa_\rho} \simeq \frac{\langle u_1 u_3\rangle}{\partial\langle U_1\rangle/\partial x_3} \cdot \frac{\partial\langle\theta\rangle/\partial x_3}{\langle\theta' u_3\rangle}. \quad (34)$$

The value of Pr_T is known to be close to unity, but there is no consensus on what the specific neutral value of Pr_T should be. Data from stably stratified flows suggest values of Pr_T in the range 0.5–1.0 for neutrally stratified flows (see, e.g., Venayagamoorthy and Stretch 2010, and therein references). The profiles of Pr_T measured in the present study are shown in Fig. 23. A strong spatial variation of Pr_T is observed. Feng et al. (2007, 2010) also report a spatial variation of measured Pr_T around 0.8. However, in our study, at the upstream of the stratified jet, Pr_T is a value ranging from 0.6 (close to the center) to 1.4 (close to the edge). At the downstream, however, difference in stable stratification and unstable stratification regions is evident. In high-*Ri* case, Pr_T ranges from 1.0 to 1.5. These results suggest that Pr_T is generally under-predicted by a value of unity and its variation across the stratified jet should be accounted.

6 Conclusion

A combined PIV-PLIF technique is developed to measure the velocity and density fields simultaneously. The illumination of PIV particles and excitation of PLIF dye are achieved by a dual-head pulsed Nd:YAG laser and two CCD cameras with a set of optical filters. The procedure

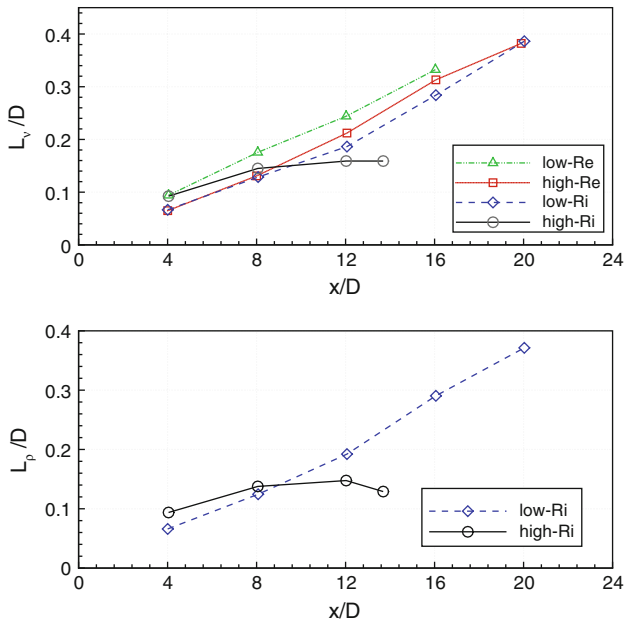

Fig. 22 Development of (*top*) $\mathcal{L}_v$ and (*bottom*) $\mathcal{L}_\rho$ at different downstream locations

for matching refractive indexes of different fluids and calibration of the combined system are presented, as well as a quantitative analysis of the measurement uncertainties. This system is applied to study a stratified jet problem, in which a round liquid jet with larger density is injected horizontally into a tank filled with light fluid. Stable stratification and unstable stratification are present in this setup. The interplay of turbulent effect and buoyancy effect can be studied by adjusting the Reynolds and Richardson numbers. The measurements are performed at different downstream locations starting from the near-nozzle region where the flow is not fully developed.

The developments of mean parameters reveal structures of the stratified jet. Stable stratification reduces mixing and unstable stratification enhances mixing. This results in asymmetry of the jet profiles (velocity and density). The decay of $U_c(x)$ (horizontal velocity peak) is dependent on *Re* only, whereas the development of $W_c(x)$ (vertical velocity component) is governed by *Ri*. Examinations of *z*-profiles at low-*Ri* and high-*Ri* cases show a strong correlation between $\langle u_1 u_3 \rangle$ and $\langle \theta' u_3 \rangle$. This may lead to important implication in modeling these two terms in turbulent closure models and need to be systematically studied. The present data also helps to examine the budget of turbulent kinetic energy. The buoyancy flux term ($\mathcal{B}$) is of positive (negative) value in stable (unstable) stratification region, and the magnitude of $\mathcal{B}$ is significantly less than those of turbulent production ($\mathcal{P}$) and dissipation rate (ϵ). $\mathcal{P}$ in the stable stratification region is significantly larger than its value in unstable stratification region. In stable

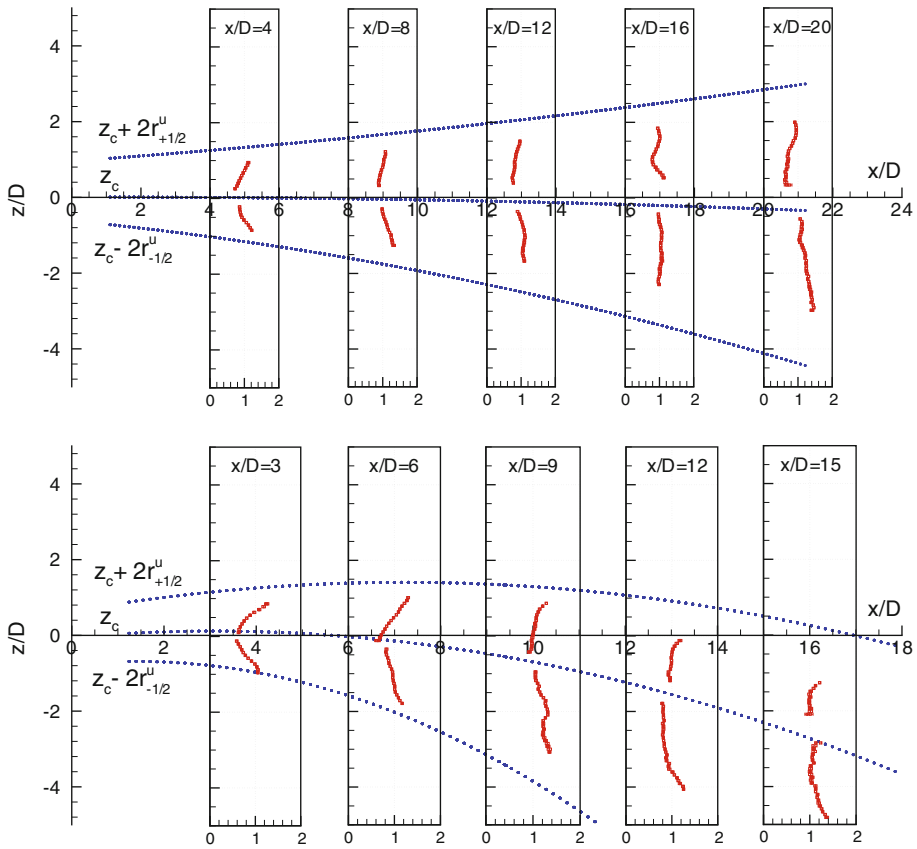

Fig. 23 Development of Pr_T as function of *x*: (*top*) low-*Ri* case and (*bottom*) high-*Ri* case. *Dash lines* show the center (z_c) as well as the outer edges ($z_c \pm 2r^u_{\pm 1/2}$) of the stratified jet. The maximum uncertainty of measured Pr_T is estimated as ± 0.07 with a level of confidence of 95%

stratification region, most of $\mathcal{P}$ is consumed by mean-flow convection $\partial T_j/\partial x_j$, whereas in unstable stratification region, we observe $\mathcal{P} \simeq \epsilon$. These observations suggest a need to revisit the fundamental assumption of balanced $\mathcal{P}$ and ϵ used in developing turbulent closure models for geophysical flows (e.g., Mellor and Yamada 1974, 1982). The difference of stable stratification and unstable stratification should be considered in determining appropriate models. The experimental data also indicate that mixing length model performs better in stable stratification regions (in the mixing zone of the jet) in modeling $\langle u_1 u_3 \rangle$ and $\langle \theta' u_3 \rangle$, with $\mathcal{L}_v \simeq \mathcal{L}_\rho$ in both stratified cases. In other regions, eddy viscosity/diffusivity models with static model coefficients give better representation of $\langle u_1 u_3 \rangle$ and $\langle \theta' u_3 \rangle$. Experimental data also show strong spatial variation of turbulent Prandtl number Pr_T. At downstream of the stratified jet the commonly adopted value of Pr_T (between 0.5 and 1.0) is less than the measured values.

The experiments describe in this paper establish a benchmark test case of stratified flows for studying the underlying physics as well as testing numerical models. Ongoing efforts include systematic study of $Ri-Re$ dependence of mixing and entrainment in stratified flows using data collected from this model problem, as well as examination of advanced closure models.

References

Alahyari A, Longmire EK (1994) Particle image velocimetry in a variable density flow: application to a dynamically evolving microburst. Exp Fluids 17:434–440

Bacon S (1998) Decadal variablity in the outflow from the Nordic seas to the deep Atlantic ocean. Nature 394:871–874

Baines PG (2001) Mixing in flows down gentle slopes into stratified environment. J Fluid Mech 443:237–270

Baines PG (2002) Two-dimensional plumes in stratified environments. J Fluid Mech 471:315–337

Baines PG (2005) Mixing regimes for the flow of dense fluid down slopes into stratified environment. J Fluid Mech 538:245–267

Borg A, Bolinder J, Fuchs L (2001) Simultaneous velocity and concentration measurements in the near field of a turbulent low-pressure jet by digital particle image velocimetry-planar laser-induced fluorescence. Exp Fluids 31:140–152

Chen J, Meneveau C, Katz J (2006) Scale interactions of turbulence subjected to a straining-relaxation-destraining cycle. J Fluid Mech 562:123–150

Chen J, Odier P, Rivera M, Ecke R (2007) Laboratory measurement of entrainment and mixing in oceanic overlfows. In: Proceedings of 2007 joint ASME/JSME fluids engineering summer conference, San Diego, CA, USA

Cowen EA, Chang KA, Liao Q (2001) A single-camera coupled PTV-LIF technique. Exp Fluids 31:63–73

Crimaldi JP (1997) The effect of photobleaching and velocity fluctuations on single-point LIF measurements. Exp Fluids 23:325–330

Crimaldi JP (2008) Planar laser induced fluorescence in aqueous flows. Exp Fluids 44:851–863

Crimaldi JP, Koseff JR (2001) High-resolution measurements of the spatial and temporal scalar structure of a turbulent plume. Exp Fluids 31:90–102

Dahm WJA, Dimotakis PE (1987) Measurements of entrainment and mixing in turbulent jets. AIAA J 25:1216–1223

Daviero GJ, Roberts PJW, Maile K (2001) Refractive index matching in large-scale stratified experiments. Exp Fluids 31:119–126

de Jong J, Cao L, Woodward SH, Salazar JPLC, Collins LR, Meng H (2009) Dissipation rate estimation from piv in zero-mean isotropic turbulence. Exp Fluids 46:499–515

Doron P, Bertuccioli L, Katz J, Osborn T (2001) Turbulence characteristics and dissipation estimates in the costal ocean bottom boundary layer from PIV data. J Phys Oceanogr 31:2108–2134

Du H, Fuh RA, Li J, Corkan A, Lindsey JS (1998) PhotochemCAD: a computer-aided design and research tool in photochemistry. Photochem Photobiol 68:141–142

Ellison TH, Turner JS (1959) Turbulent entrainment in stratified flows. J Fluid Mech 6:423–448

Feng H, Olsen MG, Hill JC, Fox RO (2007) Simultaneous velocity and cocentration field measurements of passive-scalar mixing in a confined rectangular jet. Exp Fluids 42:847–862

Feng H, Olsen MG, Hill JC, Fox RO (2010) Investigation of passive scalar mixing in a confined rectangular wake using simultaneous PIV and PLIF. Chem Eng Sci 65:3372–3383

Hallworth MA, Phillips JC, Huppert HE, Stephen R, Sparks J (1993) Entrainment in turbulent gravity currents. Nature 362:829–831

Hannoun I, Fernando H, List E (1988) Turbulent structure near a sharp density interface. J Fluid Mech 189:189–209

Hansen B, Østerhus S (2000) North Atlantic-Nordic seas exchange. Prog Oceanogr 45:109–208

Hinze JO (1987) Turbulence. McGraw-Hill, New York

Hjertager LK, Hjertager BH, Deen NG, Solberg T (2003) Measurement of turbulent mixing in a confined wake flow using combined PIV and PLIF. Can J Chem Eng 81:1149–1158

Horner-Devine AR (2006) Velocity, density and transport measurements in rotating, stratified flows. Exp Fluids 41:559–571

Huang H, Dabiri D, Gharib M (1997) On errors of digital particle image velocimetry. Meas Sci Technol 8:1427–1440

Hult EL, Troy CD, Koseff JR (2009) The breaking of interfacial waves at a submerged bathymetric ridge. J Fluid Mech 637:45–71

Ivey GN, Winters KB, Koseff JR (2008) Density stratification, turbulence, but how much mixing. Ann Rev Fluid Mech 40:169–184

Keane RD, Adrian RJ (1990) Optimization of particle image velocimeters. part 1: double pulsed systems. Meas Sci Technol 1:1202–1215

Kneller BC, Bennett SJ, McCaffrey WD (1999) Velocity structure, turbulence and fluid stresses in experimental gravity current. J Geophys Res 104:5381–5391

Kwon SJ, Seo IW (2005) Reynolds number effects on the behavior of a non-buoyant round jet. Exp Fluids 38:801–812

Large WG, McWilliams JC, Doney SC (1994) Oceanic vertical mixing: a reivew and a model with nonlocal boundary layer parameterization. Rev Geophys 32:363–403

Lowe RJ, Linden PF, Rottman JW (2002) A laboratory study of the velocity structure in an intrusive gravity current. J Fluid Mech 456:33–48

McDougall T (1979) On the elimination of refractive-index variations in turbulent density-stratified liquid flows. J Fluid Mech 93:83–96

Mehta RD, Bradshaw P (1979) Design rules for small low speed wind tunnels. Aeronaut J Aeronaut Soc 73:443–449

Mellor GL, Yamada T (1974) A hierarchy of turbulence closure models for planetary boundary layers. J Atmos Sci 31:1791–1806

Mellor GL, Yamada T (1982) Development of a turbulence closure model for geophysical fluid problems. Rev Geophys Space Phys 20(4):851–875

Muller P, Garrett C (2002) From stirring to mixing in a stratified ocean. Oceanography 15:12–19

Odier P, Chen J, Rivera M, Ecke R (2009) Mixing in stratified gravity currents: Prandtl mixing length. Phys Rev Lett 102:134,504

Papanicolaou P, List EJ (1998) Investigations of round vertical turbulent buoyant jets. J Fluid Mech 195:341–391

Pope SB (2001) Turbulent flows. Cambridge University Press, Cambridge

Pouliquen O, Chomaz JM, Huerre P (1994) Propagating holmboe waves at the interface between two immiscible fluids. J Fluid Mech 226:277–302

Raffel M, Willert C, Wereley S, Kompenhans J (2007) Particle image velocimetry—a practical guide. 2nd edn. Springer, Berlin

Simpson J (1997) Gravity currents: in the environment and the laboratory. 2nd edn. Cambridge University Press, Cambridge

Smith R, Jones P, Briegleb B, Bryan F, Danabasoglu G, Dennis J, Dukowicz J, Eden C, Fox-Kemper B, Gent P, Hecht M, Jayne S, Jochum M, Large W, Lindsay K, Maltrud M, Norton N, Peacock S, Vertenstein M, Yeager S (2010) The Parrallel Ocean Program (POP) reference manual—ocean component of the community climate system model (ccsm) and community earth system model (cesm). Technical Report LAUR-10-01853 (Los Alamos National Laboratory)

Spedding GR (1997) The evolution of initially turbulent bluff-body wakes at high internal froude number. J Fluid Mech 337:283–301

Spedding GR, Browand FK, Fincham AM (1996) Turbulence, similarity scaling and vortex geometry in the wake of a towed sphere in a stably stratified fluid. J Fluid Mech 314:53–103

Stretch DD, Rottman JW, Venayagamoorthy SK, Nomura KK, Rehmann CR (2010) Mixing efficiency in decaying stably stratified turbulence. Dyn Atmos Oceans 49:25–36

Sutherland BR (2002) Interfacial gravity currents. I. mixing and entrainment. Exp Fluids 14:2244–2254

Thomas PJ, Linden PF (2007) Rotating gravity currents: small-scale and large-scale laboratory experiments and geostrophic model. J Fluid Mech 578:35–65

Thorpe SA (2007) An introduction to ocean turbulence. Cambridge University Press, Cambridge

Troy C, Koseff J (2005) The generation and quantitative visualization of breaking internal waves. Exp Fluids 38:549–562

Turner JS (1973) Buoyancy effects in fluids. Cambridge University Press, Cambridge

Turner JS (1986) Turbulent entrainment: the development of the entrainment assumption, and its application to geophysical flows. J Fluid Mech 173:431–471

Venayagamoorthy SK, Stretch DD (2010) On the turbulent prandtl number in homogeneous stably stratified turbulence. J Fluid Mech 644:359–369

Wang H (2000) Investigations of buoyant jet discharges using combined dpiv and plif. PhD thesis, Nanyang Technological University, Singapore

Webster DR, Liu Y (2001) Velocity measurements of turbulence collapse in a linearly stratified jet. Exp Fluids 31:394–400